TU Delft

Delft University of Technology

Computation of ultrasound propagation in a population of nonlinearly oscillating microbubbles including multiple scattering

Matalliotakis, A.; Verweij, M. D.

DOI
10.1121/10.0017770

Publication date
2023

Document Version
Final published version

Published in
Journal of the Acoustical Society of America

Citation (APA)
Matalliotakis, A., & Verweij, M. D. (2023). Computation of ultrasound propagation in a population of nonlinearly oscillating microbubbles including multiple scattering. *Journal of the Acoustical Society of America*, *153*(4), 2209-2222. https://doi.org/10.1121/10.0017770

Important note
To cite this publication, please use the final published version (if applicable).
Please check the document version above.

Copyright
Other than for strictly personal use, it is not permitted to download, forward or distribute the text or part of it, without the consent of the author(s) and/or copyright holder(s), unless the work is under an open content license such as Creative Commons.

Takedown policy
Please contact us and provide details if you believe this document breaches copyrights.
We will remove access to the work immediately and investigate your claim.

This work is downloaded from Delft University of Technology.
For technical reasons the number of authors shown on this cover page is limited to a maximum of 10.

APRIL 11 2023

Computation of ultrasound propagation in a population of nonlinearly oscillating microbubbles including multiple scattering

A. Matalliotakis; M. D. Verweij

Check for updates

J Acoust Soc Am 153, 2209 (2023)
https://doi.org/10.1121/10.0017770

View Online
Export Citation
CrossMark

Related Content

The iterative nonlinear contrast source method for simulating ultrasound propagation through a polydisperse microbubble population

J Acoust Soc Am (April 2021)

Simulating multiple scattering inside a population of nonlinearly oscillating microbubbles using the Iterative Nonlinear Contrast Source method

J Acoust Soc Am (October 2022)

Modulational instability of microbubbles surface modes

AIP Conference Proceedings (May 2012)

Downloaded from http://pubs.aip.org/asa/jasa/article-pdf/153/4/2209/16822279/2209_1_10.0017770.pdf

Take the Lead in Acoustics
The ability to account for coupled physics phenomena lets you predict, optimize, and virtually test a design under real-world conditions – even before a first prototype is built.
» Learn more about COMSOL Multiphysics®
COMSOL

JASA ARTICLE

Computation of ultrasound propagation in a population of nonlinearly oscillating microbubbles including multiple scattering

A. Matalliotakis[a] and M. D. Verweij[b]
Section of Medical Imaging, Department of Imaging Physics, Faculty of Applied Sciences, Delft University of Technology, 2628 CJ Delft, The Netherlands

ABSTRACT:
In contrast-enhanced echography, the simulation of nonlinear propagation of ultrasound through a population of oscillating microbubbles imposes a computational challenge. Also, the numerical complexity increases because each scatterer has individual properties. To address these problems, the Iterative Nonlinear Contrast Source (INCS) method has been extended to include a large population of nonlinearly responding microbubbles. The original INCS method solves the Westervelt equation in a four-dimensional spatiotemporal domain by generating increasingly accurate field corrections to iteratively update the acoustic pressure. The field corrections are computed by the convolution of a nonlinear contrast source with the Green's function of the linear background medium. Because the convolution integral allows a coarse discretization, INCS can efficiently deal with large-scale problems. To include a population of microbubbles, these are considered as individual contrast point sources with their own nonlinear response. The field corrections are computed as before, but now, in each iteration, the temporal signature of each contrast point source is computed by solving the bubble's Marmottant equation. Physically, each iteration adds an order of multiple scattering. Here, the performance of the extended INCS method and the significance of multiple scattering is demonstrated through various results from different configurations.
© *2023 Author(s). All article content, except where otherwise noted, is licensed under a Creative Commons Attribution (CC BY) license (http://creativecommons.org/licenses/by/4.0/).* https://doi.org/10.1121/10.0017770
(Received 15 November 2022; revised 17 March 2023; accepted 17 March 2023; published online 11 April 2023)
[Editor: Charles C. Church] Pages: 2209–2222

I. INTRODUCTION

For several decades, encapsulated microbubbles containing gas have been widely used in medical echography as the primary ultrasound contrast agents (UCA).[1] These spherical bubbles are injected intravenously and have a size comparable to a red blood cell, which allows them to travel even in the smallest blood vessels. To avoid dissolution in the blood, they are usually coated with a shell made from phospholipid, denatured human serum albumin, or polymer. An important property is that they resonate in the same frequency range as used for ultrasound imaging. Moreover, due to their large difference in acoustic impedance with the surroundings and their highly nonlinear oscillatory behavior,[2] microbubbles scatter sound efficiently in their fundamental and harmonic modes. Through multiple studies, the dynamics of a single bubble are well understood. However, understanding the behavior of a bubble cloud is much more challenging and is partly still unknown, especially when multiple scattering must be considered.

Because of the significance in various marine settings, multiple studies were focused on the acoustic propagation of sound in bubbly liquids.[3] Justified by the small gas volume fraction, an effective medium theory[4–7] was established. This implies that the contribution of the interactions between the scatterers was considered unimportant. Initially, a set of averaged equations was constructed in a heuristic way,[8] which later was established by a more mathematically systematic approach.[9] Improvements were made for linear scatterers in small concentrations, retaining the hypothesis of effective medium.[10–12]

A study focusing on smaller bubbles in the regime of ultrasound frequencies,[13] however, showed that experimental results did not agree with effective medium theory. Therefore, the acoustic response of populations with a high concentration of nonlinear scatterers were investigated analytically.[14,15] When second-order multiple scattering is taken into account, attenuation at the resonance frequency is increased.[16] The significance of the latter was reinforced computationally by introducing nonlinear monodisperse[17] and polydisperse[18,19] microbubbles in a finite difference scheme. These studies assumed a collective behavior of the bubbles, which prohibits them to have an independent response due to having individual properties. Finally, a plethora of groups directed their attention to simplified simulations of multiple bubble interactions inside a one-dimensional or two-dimensional domain.[20,21] One of the studies was able to successfully model the nonlinear propagation

[a]Electronic mail: a.matalliotakis@tudelft.nl
[b]Also at: Section of Biomedical Engineering, Department of Cardiology, Erasmus MC University Medical Center, 3000 CA Rotterdam, The Netherlands.

Downloaded from http://pubs.aip.org/asa/jasa/article-pdf/153/4/2209/16822279/2209_1_10.0017770.pdf

of ultrasound through a uniform distribution of microbubbles, but was limited to two dimensions due to computational cost.[22]

In this article, we will employ the Iterative Nonlinear Contrast Source (INCS) method[23,24] to tackle the challenge of numerically simulating the nonlinear response of a three-dimensional (3D) bubble population with significant multiple scattering, as outlined in Fig. 1. This method was originally invented to accurately calculate the cumulative nonlinear effects suffered by an acoustic pressure wave propagating in a fluid with nonlinear medium behavior. The pressure wave originated from a source aperture with a pulsed excitation in a 3D spatial domain. A significant advantage of this algorithm is the coarse discretization of two points per shortest desired wavelength. This is achieved by applying the Filtered Convolution (FC) approach,[25] which implies that during the computations, the spatial and temporal spectra are consistently cut off at the predetermined Nyquist limit of the highest desired frequency. This also makes that INCS can reliably deal with stronger nonlinearities causing relatively strong harmonic components. The directional independence of the nonlinear operation is another benefit that is not common to many other nonlinear computational codes. Furthermore, INCS can be easily expanded to include attenuation and inhomogeneous medium parameters of all kinds, provided these can be cast in the form of a so-called contrast source.[26–30] This also offers an opportunity for incorporating bubble inclusions. Added to its ability to address large-scale problems, INCS seems a good basis to simulate the acoustic response of microbubble populations with high accuracy and relatively low computational cost.

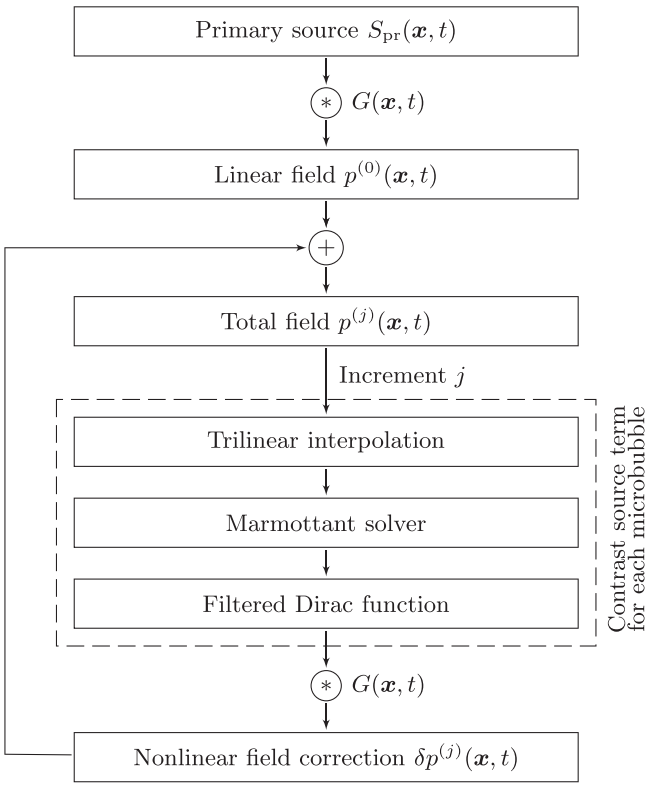

FIG. 1. Schematic diagram for the INCS method with extension to deal with microbubbles.

This article will describe the extension of the INCS method to deal with a population of scatterers. The performance of the developed method will also be demonstrated by showing the acoustic response of a population of microbubbles that oscillate in a nonlinear way, as described by the Marmottant model.[31] The method computes the scattered pressure from the cloud in an iterative way. Numerically, each iteration brings the answer closer to the exact result. Physically, each iteration accounts for an extra order of multiple scattering. To focus on the influence and behavior of the microbubble cloud, it will be assumed that the embedding fluid is linear.

First, in Sec. II, the fundamental theory behind the INCS method will be described. In Sec. III, the INCS method will be extended by the introduction of point contrast sources representing point scatterers. The representation of a linearly scattering sphere by a point scatterer is discussed, followed by the representation of a nonlinear microbubble, and last the representation of an entire population of microbubbles. In Sec. IV, the details of the numerical implementation of the method are described. Next, in Sec. V, the results from the numerical simulations for a monodisperse microbubble population are presented and explained. Concluding remarks are given in Sec. VI.

II. FUNDAMENTALS OF INCS

A. Linear field

In a lossless, linear, isotropic, and homogeneous acoustic background medium, the pressure field generated by an external or primary source can be described by the wave equation

$$c_0^{-2}\frac{\partial^2 p(\boldsymbol{x},t)}{\partial t^2}-\nabla^2 p(\boldsymbol{x},t)=S_{\mathrm{pr}}(\boldsymbol{x},t), \tag{1}$$

where $\boldsymbol{x}$ [m] is the position vector of a point in 3D Cartesian space, t [s] is the time, and $p(\boldsymbol{x},t)$ [Pa] is the acoustic pressure. The medium is characterized by the small signal speed of sound $c_0=1/\sqrt{\rho_0\kappa_0}$ [m/s], the mass density ρ_0 [kg/m^3], and the compressibility κ_0 [Pa^{-1}]. The symbol ∇^2 indicates the Laplace operator. The right hand side of Eq. (1) is the primary source term

$$S_{\mathrm{pr}}(\boldsymbol{x},t)=\rho_0\frac{\partial q(\boldsymbol{x},t)}{\partial t}-\nabla\cdot\boldsymbol{f}(\boldsymbol{x},t), \tag{2}$$

where $q(\boldsymbol{x},t)$ [s^{-1}] is the volume injection rate density and $\boldsymbol{f}(\boldsymbol{x},t)$ [N/m^3] is the volume force density of the external source. Sources with a plane aperture, such as a phased array transducer, can be represented either by a velocity or a pressure jump condition in the transducer plane $z=0$.

In INCS, and throughout this paper, the explicit solution for the pressure field due to any source $S(\boldsymbol{x},t)$ in the

Downloaded from http://pubs.aip.org/asa/jasa/article-pdf/153/4/2209/16822279/2209_1_10.0017770.pdf

https://doi.org/10.1121/10.0017770

background medium is denoted as $p(\boldsymbol{x},t)=\mathcal{G}[S]$. The symbol $\mathcal{G}$ indicates the linear operation defined by

$$\begin{aligned}\mathcal{G}[S] &= S(\boldsymbol{x},t)*_{\boldsymbol{x},t}G(\boldsymbol{x},t)\\ &= \int_{\mathcal{T}}\int_{\mathcal{X}} S(\boldsymbol{x}',t')\,G(\boldsymbol{x}-\boldsymbol{x}',t-t')\,d\boldsymbol{x}'dt'.\end{aligned} \tag{3}$$

The symbol $*_{\boldsymbol{x},t}$ denotes a convolution in the spatiotemporal domain, where the integration takes place over the spatial domain $\mathcal{X}$ and over the temporal domain $\mathcal{T}$ of the source S. The three-dimensional Green's function of the lossless, linear, homogeneous, and isotropic background medium is denoted as $G(\boldsymbol{x},t)$ and is given by

$$G(\boldsymbol{x},t)=\frac{\delta(t-||\boldsymbol{x}||/c_0)}{4\pi||\boldsymbol{x}||}. \tag{4}$$

In the numerator, δ is the Dirac delta distribution and $||\boldsymbol{x}||$ is the length of $\boldsymbol{x}$. In physical terms, the Green's function is the acoustic pressure at field point $\boldsymbol{x}$ and time t, emitted from a point source of unit impulse located at $(x,y,z)=(0,0,0)$, acting at $t=0$.[32]

The linear acoustic pressure distribution due to the primary source, e.g., an emitting transducer, in the background medium is indicated as $p^{(0)}$. With the notation presented above, it is given by

$$p^{(0)}=\mathcal{G}[S^{(0)}], \tag{5}$$

where $S^{(0)}=S_{\mathrm{pr}}$. The field $p^{(0)}$ is the initial field for the Neumann iterative scheme that is used to compute the nonlinear field contribution.

B. Nonlinear field

In medical diagnostics, the propagation of the pressure wave is dependent on the nonlinear behaviour of the medium. If the so-called local nonlinearities are neglected, the remaining global nonlinearities can be accounted for by extending Eq. (1) to the Westervelt equation.[33] In INCS, the lossless form of the Westervelt equation is written as

$$c_0^{-2}\frac{\partial^2 p}{\partial t^2}-\nabla^2 p=S_{\mathrm{pr}}+S_{\mathrm{nl}}, \tag{6}$$

where the nonlinear term is given by

$$S_{\mathrm{nl}}(p)=\frac{\beta}{\rho_0 c_0^4}\frac{\partial^2 p^2}{\partial t^2}, \tag{7}$$

in which β is the coefficient of nonlinearity. The term in Eq. (7) is considered to describe a nonlinear contrast source acting in the linear background medium. As such, it provides the nonlinear contribution to the acoustic pressure field, which can be expressed as $\delta p=\mathcal{G}[S_{\mathrm{nl}}(p)]$ with $\mathcal{G}$ being the same linear operator as in Eq. (3) but with integrations running over the entire spatiotemporal support $\mathcal{X}_{\mathrm{nl}}\times\mathcal{T}_{\mathrm{nl}}$ of S_{nl}. Often, this is the entire computational domain. However, combining Eqs. (6) and (7) yields an implicit solution because the total field p is not yet known. To obtain an explicit solution, an iterative approach is employed in which a nonlinear correction $\delta p^{(j)}$ is obtained from the previous approximation $p^{(j-1)}$ of the total field, according to

$$S_{\mathrm{nl}}^{(j)}=S_{\mathrm{nl}}(p^{(j-1)}), \tag{8}$$

$$\begin{aligned}\delta p^{(j)} &= \mathcal{G}\left[S_{\mathrm{nl}}^{(j)}\right]\\ &= \int_{\mathcal{T}_{\mathrm{nl}}}\int_{\mathcal{X}_{\mathrm{nl}}} S_{\mathrm{nl}}^{(j)}(\boldsymbol{x}',t)\,G(\boldsymbol{x}-\boldsymbol{x}',t-t')\,d\boldsymbol{x}'dt,\end{aligned} \tag{9}$$

$$p^{(j)}=p^{(0)}+\delta p^{(j)}. \tag{10}$$

To get a first estimate of the nonlinear correction, the initially computed linear pressure field $p^{(0)}$ is used in the contrast source term. The resulting Neumann iterative scheme can thus be expressed as

$$p^{(0)}=\mathcal{G}[S_{\mathrm{pr}}], \tag{11}$$

$$p^{(j)}=p^{(0)}+\mathcal{G}\left[S_{\mathrm{nl}}(p^{(j-1)})\right]\quad \text{if } j\geq 1. \tag{12}$$

Using the same methodology, INCS has been extended by the inclusion of other contrast sources, e.g., representing attenuation and inhomogeneous medium properties.[26–30]

III. INCLUSION OF MICROBUBBLES

A. Contrast source term representing a point scatterer

In this section, we will extend INCS to deal with a medium containing a large population of microbubbles. Because a microbubble is much smaller than the spatial grid step, we will represent each bubble by a point scatterer. A point scatterer is an object with an infinitely small volume, which is used to approximate the behavior of a scatterer that is much smaller than the wavelength of the excitation field. The analytical description of a contrast source representing a point scatterer located at point $\boldsymbol{x}_{\mathrm{sc}}$ and with a time signature $A(\boldsymbol{x}_{\mathrm{sc}},t)$ is

$$S_{\mathrm{sc}}(\boldsymbol{x},t)=A(\boldsymbol{x}_{\mathrm{sc}},t)\delta(\boldsymbol{x}-\boldsymbol{x}_{\mathrm{sc}}). \tag{13}$$

As explained in a previous publication,[25] the INCS method applies spatial filtering with an ideal low pass filter in all dimensions to avoid aliasing during numerical computation. The spatially filtered version of the Dirac function is

$$\delta_K(\boldsymbol{x},\boldsymbol{x}_{\mathrm{sc}})=\prod_{n=1}^{3}\frac{K}{\pi}\,\mathrm{sinc}\left[K(x_n-x_{n,\mathrm{sc}})\right], \tag{14}$$

where $K=\pi/\Delta x$ is the angular spatial cutoff frequency that depends on the spatial step size Δx, and $(x_1,x_2,x_3)=(x,y,z)$ are the spatial coordinates.

A point scatterer can represent either a nonoscillating object that reflects the incoming wave because of its contrasting medium properties, or a noncontrasting object that radiates an outward wave because of its radial oscillation

Downloaded from http://pubs.aip.org/asa/jasa/article-pdf/153/4/2209/16822279/2209_1_10.0017770.pdf

induced by the incoming wave.[32] A microbubble shows contrast with its surroundings but also vibrates, so the question might arise whether both effects should be accounted for separately. To resolve this issue, in Sec. III B we will first compare the off resonance scattering from a linearly responding microbubble without a shell, as obtained from both representations. Next, we will explain how to describe a nonlinear microbubble and a distribution of microbubbles.

B. Nonoscillating contrasting sphere

As a possible model for a spherical microbubble, first, we will consider the background medium with a spherical inclusion with a fixed radius R_0, a speed of sound c_1, and a density of mass ρ_1. This sphere is insonified by a pressure wave with angular frequency ω. We assume that the radius of the sphere is much smaller than the wavelength of this wave, i.e., $R_0 \ll 2\pi c_0/\omega$, so it is allowed to consider a plane incident wave. Let us suppose that in the absence of the sphere, this wave would have a pressure amplitude $p(\boldsymbol{x}_{\rm sc},\omega)$ at the location of the center of the sphere. The scattered pressure $p_{\rm sc}$ is most easily obtained in terms of spherical harmonics. To find the dominant behavior of $p_{\rm sc}$ for small spheres and below resonance, we expand this result into a power series of R_0, and keep only the three terms that are of lowest order in R_0. These are

$$p_{\rm sc}^{\rm mono} = \frac{\omega^2 p(\boldsymbol{x}_{\rm sc},\omega)V_0}{4\pi r}\left(\frac{\rho_0}{\rho_1 c_1^2}-\frac{1}{c_0^2}\right)\exp(-ik_0 r), \quad (15)$$

$$p_{\rm sc}^{\rm dip,if} = \frac{-i\omega p(\boldsymbol{x}_{\rm sc},\omega)V_0}{4\pi r^2}\frac{3(\rho_1-\rho_0)}{c_0(\rho_0+2\rho_1)}\cos(\theta)\exp(-ik_0 r), \quad (16)$$

$$p_{\rm sc}^{\rm dip,ff} = \frac{\omega^2 p(\boldsymbol{x}_{\rm sc},\omega)V_0}{4\pi r}\frac{3(\rho_1-\rho_0)}{c_0^2(\rho_0+2\rho_1)}\cos(\theta)\exp(-ik_0 r), \quad (17)$$

where $V_0 = \frac{4}{3}\pi R_0^3$ is the volume of the sphere, $r = ||\boldsymbol{x}-\boldsymbol{x}_{\rm sc}||$, θ is the angle of observation relative to the direction of the incident wave, and $k_0 = \omega/c_0$ is the wavenumber in the background medium. Because the term in Eq. (15) decays with r^{-1} and is omnidirectional, it describes the field of a physical monopole. The other two terms depend on $\cos(\theta)$ and describe the field of a physical dipole, where Eq. (16) represents the intermediate field that decays with r^{-2}, and Eq. (17) represents the far field that decays with r^{-1}.[34] In the context of ultrasound contrast agents, it is opportune to consider an incident wave of 1 MHz propagating in a background consisting of water and impinging on a gas-filled sphere with a radius of 1 μm. It turns out that even on the surface of the sphere, the intermediate and far field dipole terms are 2 and 4 orders of magnitude smaller, respectively, than the monopole term. We conclude that in this paper, we may consider a spherical microbubble to act solely as a monopole. In that case, the point scatterer that for $r > R_0$ will cause the same pressure as in Eq. (15) is

$$S_{\rm sc}(\boldsymbol{x},\omega) = \omega^2 p(\omega)V_0\rho_0\left(\frac{1}{\rho_1 c_1^2}-\frac{1}{\rho_0 c_0^2}\right)\delta(\boldsymbol{x}-\boldsymbol{x}_{\rm sc}). \quad (18)$$

The time domain equivalent of this equation is

$$S_{\rm sc}(\boldsymbol{x},t) = -V_0\rho_0\left(\frac{1}{\rho_1 c_1^2}-\frac{1}{\rho_0 c_0^2}\right)\frac{\partial^2 p(\boldsymbol{x}_{\rm sc},t)}{\partial t^2}\delta(\boldsymbol{x}-\boldsymbol{x}_{\rm sc}). \quad (19)$$

For a fluid background medium with a gas filled sphere, it turns out that $\rho_0 c_0^2 \gg \rho_1 c_1^2$ and Eq. (19) may be approximated by

$$S_{\rm sc}(\boldsymbol{x},t) = -V_0\frac{\rho_0}{\rho_1 c_1^2}\frac{\partial^2 p(\boldsymbol{x}_{\rm sc},t)}{\partial t^2}\delta(\boldsymbol{x}-\boldsymbol{x}_{\rm sc}). \quad (20)$$

C. Oscillating noncontrasting sphere

As a second model for a spherical microbubble, we will consider the background medium with a noncontrasting, oscillating sphere with rest radius R_0. The oscillations are induced by an incident pressure wave. Again, we assume that the radius of the sphere is much smaller than the wavelengths present in the incident wave, so the external pressure experienced by the sphere is approximately homogeneous and may be taken equal to the incident pressure $p(\boldsymbol{x}_{\rm sc},t)$ at the center of the sphere. As a consequence, we may assume that the sphere will only show radial oscillations, i.e., its instantaneous shape will be fully described by a dynamic radius $R(t)$. The oscillating sphere therefore acts as a monopole source of volume injection, which is consistent with the conclusion in Sec. III B. The volume injection rate of the monopole source is $Q = dV/dt$, in which $V = \frac{4}{3}\pi R^3(t)$. Integration of Eq. (2) over the rest volume V_0 of the sphere results in a contrast source strength $S_{\rm sc} = \rho_0 dQ/dt = \rho_0 d^2V/dt^2$. The point scatterer that for $r > R$ will cause the same pressure as the oscillating sphere is

$$S_{\rm sc}(\boldsymbol{x},t) = \rho_0\frac{d^2V}{dt^2}\delta(\boldsymbol{x}-\boldsymbol{x}_{\rm sc}). \quad (21)$$

To find the relation between Eqs. (19) and (21) for linearly responding bubbles below resonance, we consider the linearized equations of motion and continuity. Inside the bubble, these may be written as

$$\nabla p + \rho_0\frac{\partial \boldsymbol{v}}{\partial t} = (\rho_0-\rho_1)\frac{\partial \boldsymbol{v}}{\partial t} + \boldsymbol{f}, \quad (22)$$

$$\nabla\cdot\boldsymbol{v} + \kappa_0\frac{\partial p}{\partial t} = (\kappa_0-\kappa_1)\frac{\partial p}{\partial t} + q. \quad (23)$$

The terms at the right-hand sides of these equations describe the sources of the scattered field. When these are point sources, or may be considered as such, the right-hand sides of Eqs. (22) and (23) represent the dipole behavior and the monopole behavior of the sphere, respectively.[34] For a nonoscillating contrasting sphere, the density of volume force $\boldsymbol{f}$ and the density of volume injection rate q are zero, and for an oscillating noncontrasting sphere, the mass density contrast $\rho_0-\rho_1$ and the compressibility contrast $\kappa_0-\kappa_1$ are zero. To obtain the same monopole scattering from a

Downloaded from http://pubs.aip.org/asa/jasa/article-pdf/153/4/2209/16822279/2209_1_10.0017770.pdf

https://doi.org/10.1121/10.0017770

nonoscillating contrasting sphere and an oscillating noncontrasting sphere, we must, therefore, have

$$(\kappa_0 - \kappa_1)\,\frac{\partial p}{\partial t} = q = \frac{1}{V_0}\,\frac{dV}{dt}, \tag{24}$$

where p is the pressure inside the sphere, which in lowest order is equal to the incident pressure $p(\boldsymbol{x}_{\rm sc}, t)$. Multiplication by $V_0\rho_0$, differentiation with respect to time, and applying the relation $\kappa = 1/(\rho c^2)$ for linear acoustics, yields

$$-V_0\,\rho_0\left(\frac{1}{\rho_1 c_1^2} - \frac{1}{\rho_0 c_0^2}\right)\frac{\partial^2 p}{\partial t^2} = \rho_0\,\frac{d^2 V_{\rm sc}}{dt^2}. \tag{25}$$

The left-hand side and right-hand side of this equation are exactly the magnitude of the scattering sources in Eqs. (19) and (21), respectively. From this, we conclude that in the linear case, the oscillating noncontrasting sphere represents the physics of the bubble equally as well as the nonoscillating contrasting sphere. In the following parts of this paper, we extrapolate this to the nonlinear case by assuming that the volume oscillations of a nonlinear bubble fully represent the intricate physics of the interior and shell of that bubble.

D. Microbubble as a point scatterer

For practical ultrasound contrast bubbles, the models in Secs. III B and III C are not accurate enough because the presence of a shell and the effect of surface tension is missing. Moreover, in medical applications, bubbles are often used near resonance, and in the nonlinear regime. To accurately represent a microbubble by a point scatterer, the applied model should be based on the following assumptions: the surrounding liquid is infinite and behaves in a Newtonian way, there is no mass or heat transfer between the medium and the gas inside the bubble, the buoyancy and gravity effects can be neglected, the wavelength of the exciting pressure field is much larger than the radius (so that the pressure has a uniform distribution over the bubble shell), and the bubble shape remains spherical through time.[1] This implies that the bubble acts as an oscillating noncontrasting monopole source. Usually, the time-dependent bubble radius is obtained by solving some variant of the Rayleigh–Plesset equation. Therefore, it is most logical to represent a microbubble by a contrast point source

$$S_{\rm sc}(\boldsymbol{x}, t) = \rho_0\,\frac{d^2 V_{\rm sc}}{dt^2}\,\delta(\boldsymbol{x} - \boldsymbol{x}_{\rm sc}). \tag{26}$$

The scatterer's volume depends on the bubble radius as a function of time, which, in our case, we will calculate by solving the Marmottant Eq. (31). This model is most applicable to describe the oscillatory behavior of lipid-encapsulated microbubbles. We emphasize that our method is not restricted to this specific model, which can be replaced by any other model that suits another type of bubbles.

The Marmottant model relates the radius of a nonlinearly oscillating microbubble to the acoustic pressure according to

$$\begin{aligned}\rho_0\left(\ddot{R}R + \frac{3}{2}\dot{R}^2\right) =& \left(P_0 + \frac{2\sigma(R_0)}{R_0}\right)\left(\frac{R_0}{R}\right)^{3\gamma}\left(1 - \frac{3\gamma\dot{R}}{c_0}\right)\\ &- P_0 - p(\boldsymbol{x}_{\rm sc}, t) - 4\mu\frac{\dot{R}}{R} - \frac{2\sigma(R)}{R}\\ &- 4\kappa_s\frac{\dot{R}}{R^2},\end{aligned} \tag{27}$$

where the quantity P_0 [Pa] is the ambient pressure, γ is the polytropic exponent of the gas encapsulated in the bubble, $p(\boldsymbol{x}_{\rm sc}, t)$ [Pa] is the excitation pressure in the surrounding liquid of the scatterer, μ [Pa · s] is the gas core viscosity, κ_s [kg/s] is the shell viscosity, and $\sigma(R)$ [N/m] is the effective surface tension. Based on the shell-buckling model of Marmottant, the latter variable is expressed as

$$\sigma(R) = \begin{cases} 0 & \text{if } R \le R_b,\\ \chi\left(\dfrac{R^2}{R_b^2} - 1\right) & \text{if } R_b < R < R_r,\\ \sigma_w & \text{if } R \ge R_r, \end{cases} \tag{28}$$

where χ [N/m] is the shell elasticity, σ_w [N/m] is the surface tension of the gas–water interface, $R_b = R_0/\sqrt{\sigma(R_0)/\chi + 1}$ is the buckling radius, and $R_r = R_b\sqrt{\sigma_w/\chi + 1}$ is the rupture radius.

The solution of the Marmottant equation is the bubble radius as a function of time. Equation (27) was solved using the Livermore Solver for Ordinary Differential Equations (LSODE) from the ODEPACK library[35] implemented in Fortran. To enhance performance and efficiency, the Marmottant model is normalized by $\varrho_* = (R - R_0)/R_0$ and $\tau_* = tf_0$, where f_0 is the center frequency of the incident pressure field. This results in $\dot{R} = R_0 f_0\, d\varrho_*/d\tau_*$ and $\ddot{R} = R_0 f_0^2\, d^2\varrho_*/d\tau_*^2$. Based on this normalization and to achieve good convergence, the absolute and relative tolerance of the solver is set at 10^{-15}.

E. Microbubble population as distribution of point scatterers

For a population of N microbubbles, all corresponding point sources should be added, resulting in the nonlinear contrast source term

$$S_{\rm cs}(\boldsymbol{x}, t) = \rho_0\sum_{i=1}^{N}\frac{d^2 V^{(i)}(\boldsymbol{x}_{\rm sc}^{(i)}, t)}{dt^2}\,\delta(\boldsymbol{x} - \boldsymbol{x}_{\rm sc}^{(i)}). \tag{29}$$

When the microbubbles are located in an otherwise linear, homogeneous, and lossless fluid medium, the nonlinear wave equation for the acoustic pressure becomes

$$c_0^{-2}\frac{\partial^2 p}{\partial t^2} - \nabla^2 p = S_{\rm pr} + S_{\rm cs}. \tag{30}$$

Downloaded from http://pubs.aip.org/asa/jasa/article-pdf/153/4/2209/16822279/2209_1_10.0017770.pdf

The solution of Eq. (30) can be obtained by the scheme in Eq. (12), provided we replace the nonlinear contrast source S_{nl} by S_{cs} in Eq. (29).

The physical interpretation of the iterative process is explained in Fig. 2. For $j = 0$, the solution of INCS in an arbitrary point $\boldsymbol{x}$ is the incident field $p^{(0)}$. This is the field that would be generated by the primary source S_{pr} in the background medium in the absence of microbubbles [Fig. 2(a)]. For $j = 1$, the scattering of $p^{(0)}$ by all microbubbles is computed and summed, resulting in the first-order field correction $\delta p^{(1)}$. This correction is added to $p^{(0)}$ to form the first-order field estimate $p^{(1)}$, which thus consists of the incident field plus the first-order scattering of all microbubbles [Fig. 2(b)]. For $j = 2$, the scattering of $p^{(1)}$ by all microbubbles is computed and summed, resulting in the second-order field correction $\delta p^{(2)}$. This correction contains both the scattering of $p^{(0)}$ and $\delta p^{(1)}$, i.e., the first- and second-order scattering of all microbubbles. It is added to $p^{(0)}$ to form the second-order field estimate $p^{(2)}$, which consists of the incident field plus the scattering of all microbubbles up until order two [Fig. 2(c)]. Continuing the iterative scheme, each iteration accounts for a next order of multiple scattering [Fig. 2(d)].

After each iteration, we compare the field $p^{(j)}$ with the field $p^{(j-1)}$, using a Relative Root Mean Square Error (RRMSE). When this error has become negligible after several iterations, we conclude that the highest order of scattering has become insignificant and will no longer influence the final result. At this point, we assume that INCS has sufficiently converged and we terminate the iterative process.

IV. NUMERICAL IMPLEMENTATION

A. Generation of the random bubble population

Our next step is to generate the positions $\boldsymbol{x}_{\text{sc}}^{(i)}$ in a 3D population of randomly located bubbles. We have implemented two approaches for the positioning of N point scatterers in a rectangular bubble domain. In both cases, a minimum distance between every two point scatterers is assumed to avoid the overlap of the physical bubbles.

The first approach is used to create a discrete uniform distribution of point scatterers over the rectangular bubble domain. This is achieved by dividing the bubble domain in N identical, smaller cubes with a prescribed minimum mutual distance, and randomly positioning one scatterer in each one of these smaller cubes.

The second approach is applied to obtain a fully random positioning of the point scatterers, with the minimum mutual distance between scatterers as the only restriction. To accomplish this, point scatterers are randomly positioned in the domain of interest. The separation of each scatterer and its closest neighbors is then determined. Those points who do not fulfill the distancing restriction, are removed from the cloud.

Realizations obtained by these two approaches are presented in Fig. 3. The location of the point scatterers in the generated clouds is independent of the location of the computational grid points. In this way, INCS can retain a coarse grid size without "discretizing" the cloud of particles. This is particularly important for large concentrations of particles.

B. Off-grid point scatterers

Due to the coarse discretization allowed by the INCS method, some scatterers will unavoidably be placed between the grid points. This causes no problem because each point scatterer is represented by its filtered version and by using Eq. (14), proper weights are assigned to all grid points. Based on previous research,[36] this methodology will provide an accurate solution.

For large bubble concentrations, this process may not be efficient. To improve the computational efficiency and reduce the memory load for large concentrations, during intermediate iterations, only a limited number of neighboring grid points is used for the filtered version of each point scatterer. In this way, the scattered pressure is accurately computed in the region where it is strongest, i.e., around each scatterer. In the final iteration, the filtered spatial Dirac function is again using all the grid points. This corrects the errors made in the intermediate iterations. The described approach significantly reduces the computation time, at a

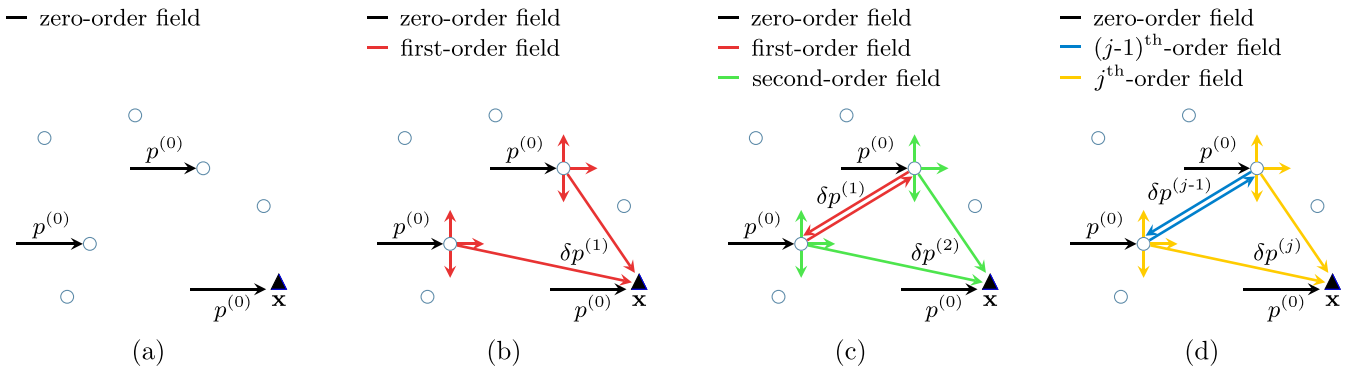

FIG. 2. (Color online) Physical interpretation of the iterative procedure for a number of scatterers (circles) and an observer **x** (triangle), after (a) 0, (b) 1, (c) 2, (d) j iterations. The black arrows represent the incident field hitting the scattterers. The colored arrows show the field corrections due to multiple scattering orders.

Downloaded from http://pubs.aip.org/asa/jasa/article-pdf/153/4/2209/16822279/2209_1_10.0017770.pdf

https://doi.org/10.1121/10.0017770

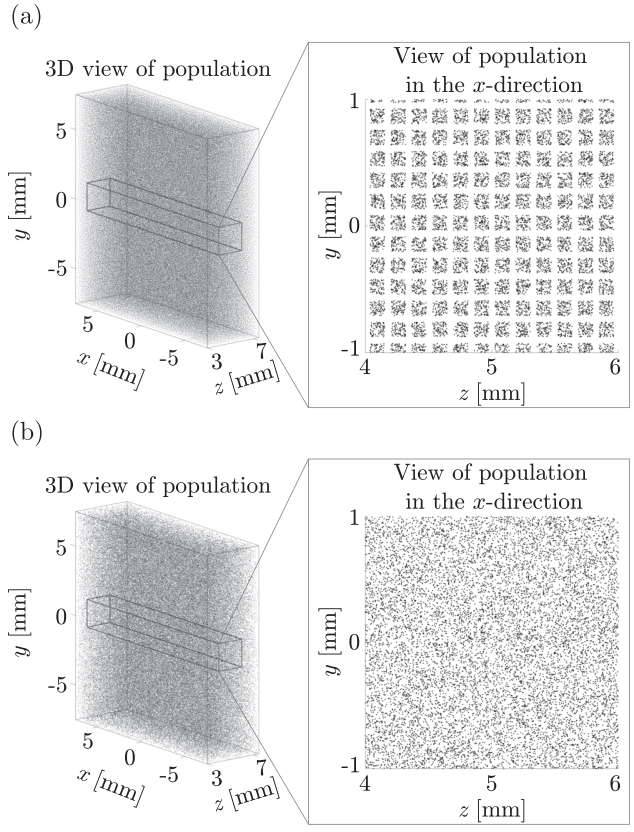

FIG. 3. (a) Uniform (a) and (b) random distribution of scatterers, shown in 3D view (left) and in the x-direction (inset, right). The populations consist of 2×10^5 scatterers concentrated in volume of 1 ml, with a minimum mutual distance of 50 μm. This distance is taken exceedingly large here to show the difference between (a) and (b).

cost of a small intermediate error. This reduction is most significant for higher concentrations. For example, we have considered a spatiotemporal computational domain with $N_t \times N_x \times N_y \times N_z = 1299 \times 200 \times 96 \times 600$ grid points, with a population of 10^6 point scatterers that are randomly positioned in a volume of 1 ml. The computational job is distributed over 100 central processing units (CPUs). The time required per iteration for computing the contrast source term in all grid points and only for a limited number of grid points around each scatterer is 91 and 10 min, respectively. The RRMSE between these cases is only 0.1%.

C. Trilinear interpolation and avoiding self-scattering

To calculate the pressure field at the off-grid location of a point scatterer, a trilinear interpolation using the eight neighboring grid points is implemented. A particular point of attention is to avoid that the pressure experienced by a point scatterer in iteration j contains the pressure that is generated by the same scatterer in iteration $j-1$. To prevent this "self-scattering", in iteration $j-1$, the computed strength of each contrast source is saved in a file. In iteration j, the point sources, represented by the filtered Dirac function, are convoluted with the Green's function to obtain the pressure generated in iteration $j-1$ by each point source at its eight neighboring grid points. These pressure values are subtracted from the total computed pressure before computing the new pressure value at the location of the point source. This correction is particularly significant for strong individual scatterers that do not have strong neighbors nearby.

V. NUMERICAL RESULTS

For the numerical examples in Secs. V A and V B, a computational domain of $X \times Y \times Z = 20\,\text{mm} \times 20\,\text{mm} \times 20\,\text{mm}$ is used. The incident pressure field is a plane wave being generated at $z = 0$ and propagating in the positive z-direction. A plane wave is used to let all the scatterers experience the same incident pressure.

In all our numerical results, the temporal signature of the incident pressure is

$$s(t) = \exp\left[-\left(\frac{t-T_d}{T_w/2}\right)^2\right]\sin[2\pi f_0(t-T_d)], \tag{31}$$

where $T_w = 3/f_0$ is the width and $T_d = 6/f_0$ is the delay of a Gaussian envelope with a duration of $12/f_0$, where $f_0 = 1\,\text{MHz}$ is the center frequency. The scatterers will be embedded in water with a density of $\rho = 1060\,\text{kg/m}^3$ and a speed of sound of $c_0 = 1482\,\text{m/s}$. In the considered situations, water has negligible losses and nonlinear effects will be hardly noticeable. Therefore, we assume that the embedding medium is lossless and linear. A sampling frequency of 18 MHz was used as the basis for the discretization of the spatiotemporal domain.

A. Single versus multiple scattering: Linear scatterers

In this subsection, we will present the difference between single and multiple scattering in case of linear scatterers. The difference will be more visible for higher concentrations. For this reason, a population of 1.6×10^6 linearly scattering spheres of 1 μm radius is placed in a subdomain $-7.50\,\text{mm} \le x \le 7.50\,\text{mm}$, $-7.50\,\text{mm} \le y \le 7.50\,\text{mm}$, $3.00\,\text{mm} \le z \le 7.44\,\text{mm}$ as indicated in Fig. 3(b). This yields a concentration of scatterers of $1.6 \times 10^6\,\text{ml}^{-1}$. It is assumed that the gas inside these scatterers is C_4F_{10}, with a density $\rho_1 = 10\,\text{kg/m}^3$ and a speed of sound $c_1 = 100\,\text{m/s}$. These spheres have a sharp resonance frequency of 2.68 MHz. The maximum of the incident pressure is $P_0 = 200\,\text{kPa}$. For first-order scattering, application of Eq. (A4) with $r = R$ then yields a maximum reflected pressure of 32.4 kPa on each individual scatterer's surface.

In Fig. 4(a), the total pressure field after $j = 1$ iterations, i.e., after accounting for one order of scattering, is presented. An increased pressure, compared to the incident wave, is visible in and behind the population of scatterers. This is due to the constructive interference of the scattering in the direction of the propagation of the plane wave, which is a consequence of Huygens's principle. In Fig. 4(b), the total pressure field for after $j = 2$ iterations, i.e., including two orders of scattering, is presented. Compared to the first iteration, the total pressure field in and behind is the population reduced and a lower pressure region starts to form

Downloaded from http://pubs.aip.org/asa/jasa/article-pdf/153/4/2209/16822279/2209_1_10.0017770.pdf

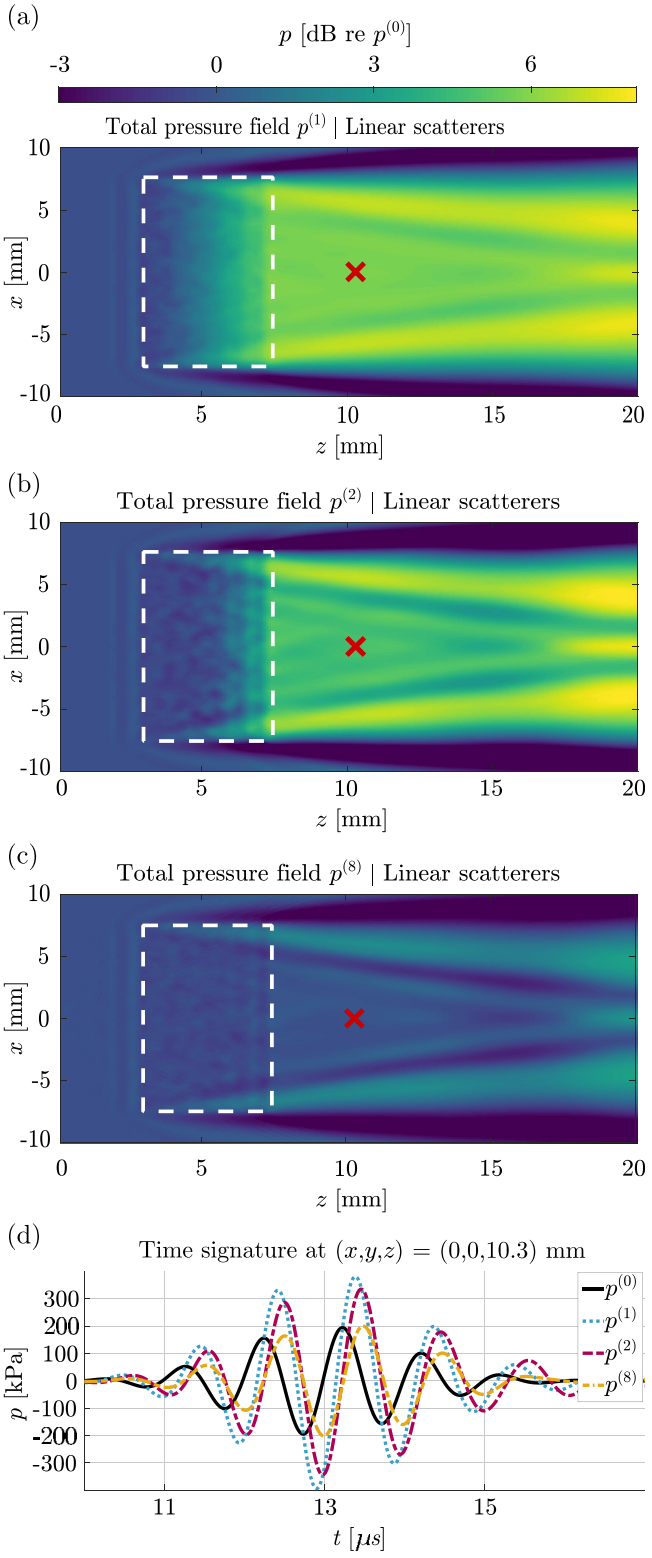

FIG. 4. (Color online) Maximum of the total pressure field in the plane $y = 0$ mm in case of 1.6×10^6 linear scatterers with 1 μm radius, when considering (a) 1, (b) 2, (c) 8 orders of scattering. The population of scatterers is inside the dotted white square. Comparison between the time signatures (d) of the total pressure pulse that is received by a point receiver located at the red cross, for a number of iterations.

behind the population. Virtually, no numerical changes occur after $j = 8$ iterations and this result is presented in Fig. 4(c). The difference between the three pressure maps is clearly visible. It can be seen that the contribution of the population is strongest in the first iteration. When more orders of multiple scattering are included, there is a correction in the total pressure field. Furthermore, it can be seen that lower pressure regions form on the sides and behind the population and become more distinct with increasing multiple scattering orders.

A comparison of the time signatures of the total pressure at a point receiver located in (0, 0, 10.3 mm) is presented in Fig. 4(d). Subtraction of $p^{(0)}$ from the other signals would result in the scattered pressure for the respective iterations. In addition to a correction of the maximum pressure, a change in phase can be seen. It seems like there is a decrease in the effective speed of sound due to the increasing scattering in the population. This figure reinforces the significance of multiple scattering and the need to consider multiple orders to have a more accurate result.

To validate our method, we can also compare the results of the above time signatures with predictions based on effective medium theory. In the current case, the conditions justify the application of the original theory of Foldy.[4] According to this theory, the effect of a monodisperse population of scatterers is represented by replacing the wave number k_0 in the scattering domain by a corrected wave number that satisfies

$$k^2 = k_0^2 + 4\pi n g, \tag{32}$$

where n is the concentration of the scatterers and g is their individual scattering strength. The shift in wavenumber corresponds to a shift in wave speed, and as a consequence, in a time shift of the wave that has traversed the scattering domain. In the case considered in this subsection, we have $n = 1.6 \times 10^{12}\,\mathrm{m}^{-3}$ and $g = 1.6218 \times 10^{-7}\,\mathrm{m}$. This yields a wavespeed of 1363.5 m/s in the scattering domain, while the speed in the medium without scatterers is 1482 m/s. Since the scattering domain has a length of 4.4444 mm, the additional time delay caused by the scattering domain, as predicted by the theory of Foldy, is $\Delta t_{\mathrm{Foldy}} = 0.2606\,\mu$s. We have also determined the time delay between the incident wave $p^{(0)}$ and the wave with all significant orders of scattering $p^{(8)}$ in Fig. 4(d), by looking at the shift in the zero crossings around 13 μs. This is found to be $\Delta t_{\mathrm{INCS}} = 0.2595\,\mu$s. Thus, the difference in time delay as predicted by the theory of Foldy and our method is only 0.42%. Moreover, because in our case, the wavenumber obtained from Eq. (32) does not contain an imaginary part, the theory of Foldy predicts that the wave that traverses the scattering domain does not attenuate. Figure 4(d) shows that our scheme corrects the larger amplitude of the earlier iterations, and that iteration $p^{(8)}$ indeed has the same amplitude as the incident field $p^{(0)}$. From the results just mentioned, we conclude that for the time delay and the amplitude of the wave traveling through a scattering domain, there is good agreement between our method and the effective medium theory of Foldy.

B. Single versus multiple scattering: Nonlinear microbubbles

Here, the same configuration as in Sec. V A is used, but now we employ the Marmottant model from Sec. III D to

Downloaded from http://pubs.aip.org/asa/jasa/article-pdf/153/4/2209/16822279/2209_1_10.0017770.pdf

https://doi.org/10.1121/10.0017770

demonstrate the difference between populations of linear and nonlinear scatterers. The concentration of the population is 2×10^5 ml^{-1} and the radius of the microbubbles is 2 μm. The parameters for the Marmottant model are given in Table I. These microbubbles also have a resonance frequency of 2.68 MHz.

In Fig. 5, the difference between $j = 1$ iteration (one order of scattering) and $j = 14$ iterations (14 orders of scattering) is shown. Compared to the population of linear scatterers, the difference between the pressure maps for subsequent iterations is more significant for the population of microbubbles. This is because the microbubbles are stronger scatterers than the linear scatterers. Virtually, no numerical changes now occur after $j = 14$ iterations. This shows that for the stronger nonlinear scatterers, more iterations should be considered. As in Sec. V A, lower pressure regions also exist in the microbubble case. Compared to the linear case, these regions are also wider, i.e., relatively more scattering energy is concentrated in the regions behind the horizontal edges of the population.

A comparison between the time signatures at the point receiver is presented in Fig. 5(c). A strong negative pressure dip can be seen when only the first order scattering is included. In addition to a correction of the maximum pressure, a change in phase is visible in the early part of the pulses. For later times, the signals from subsequent iterations become incoherent due to the nonlinear multiple scattering contributions. The frequency spectrum of the pulses is presented in Fig. 5(d). As expected, higher harmonics caused by the nonlinear behavior of the microbubbles are visible. A significant observation is that for $j = 1$, there is a dip in the fundamental and the higher harmonics are relatively strong, whereas for $j = 14$ orders, the fundamental is partly restored and the higher harmonics have decreased. These results demonstrate that multiple scattering inside a population of nonlinear scatterers plays an important role.

C. Harmonic imaging

In the previous subsection, we have shown the difference between a population of linear and nonlinear scatterers when excited by a plane wave. In this subsection, we will focus on a medical application and will demonstrate the generation of higher harmonics when a population of bubbles is hit by an ultrasound beam. Here, a computational domain of $X \times Y \times Z = 22\,\text{mm} \times 10\,\text{mm} \times 60\,\text{mm}$ is used. The incident beam is generated by a phased array transducer of 40 elements with $H_{el} \times W_{el} = 10\,\text{mm} \times 0.45\,\text{mm}$, and a kerf with zero width. This corresponds to an aperture with a width of $W_{\text{arr}} = 18\,\text{mm}$. The origin of the coordinate system is at the center of the transducer aperture. The array has an azimuthal focus at $(x_f, z_f) = (0\,\text{mm}, 35\,\text{mm})$ and an elevation focus at $z_{el} = z_f$. In Fig. 6(a), a sketch of the geometry of the phased array is presented. The pressure pulse sent from each element of the transducer is again given by Eq. (31).

TABLE I. Parameters of the Marmottant model of the applied microbubbles.

κ_s [kg/s]	σ_w [N/m]	σ_R [N/m]	γ	χ [N/m]	μ [Pa · s]
3×10^{-8}	0.072	0.036	1.07	0.4	2×10^{-3}

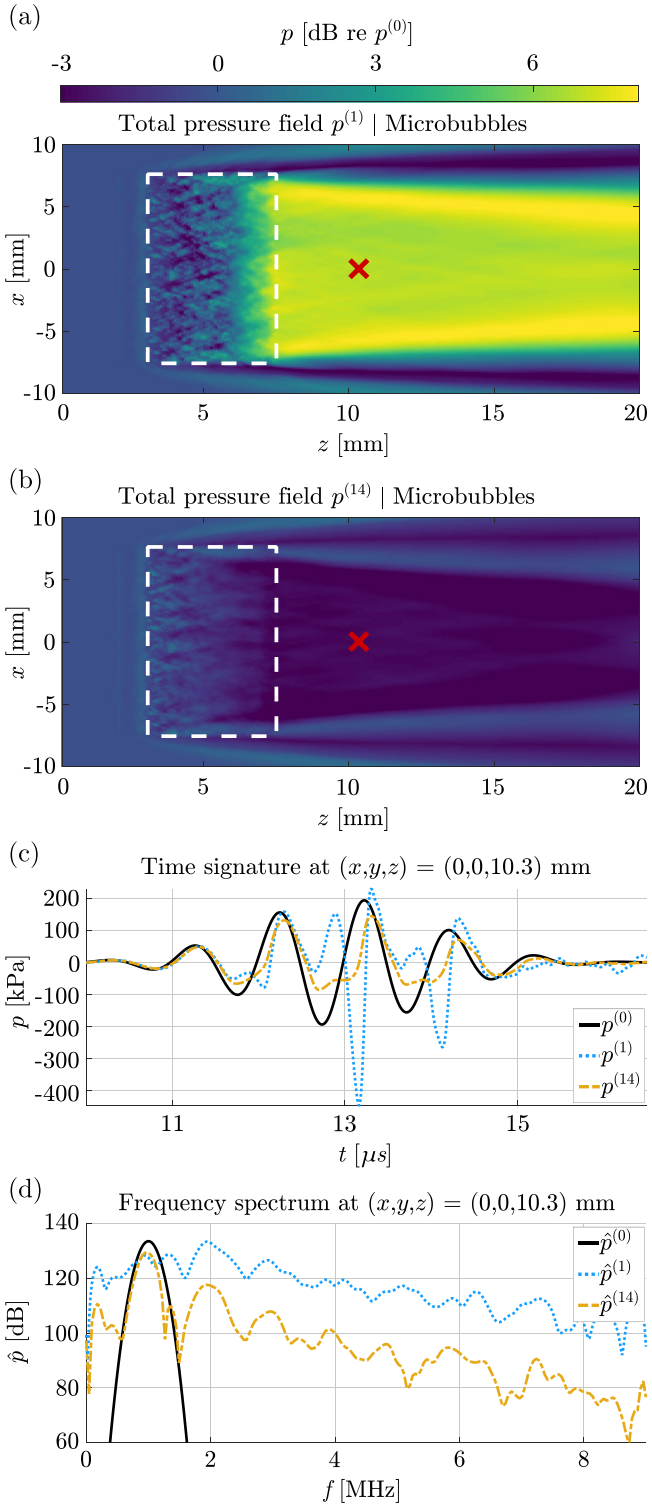

FIG. 5. (Color online) Maximum of the total pressure field in the plane $y = 0$ mm in case of 2×10^5 nonlinear microbubbles with 2 μm radius, when considering (a) 1, (b) 14, and orders of scattering. The microbubble population is inside the dotted white rectangle. Comparison between the (c) time signatures and the (d) frequency spectrum of the total pressure pulse that is received by a point receiver located at the red cross, for a number of iterations.

Downloaded from http://pubs.aip.org/asa/jasa/article-pdf/153/4/2209/16822279/2209_1_10.0017770.pdf

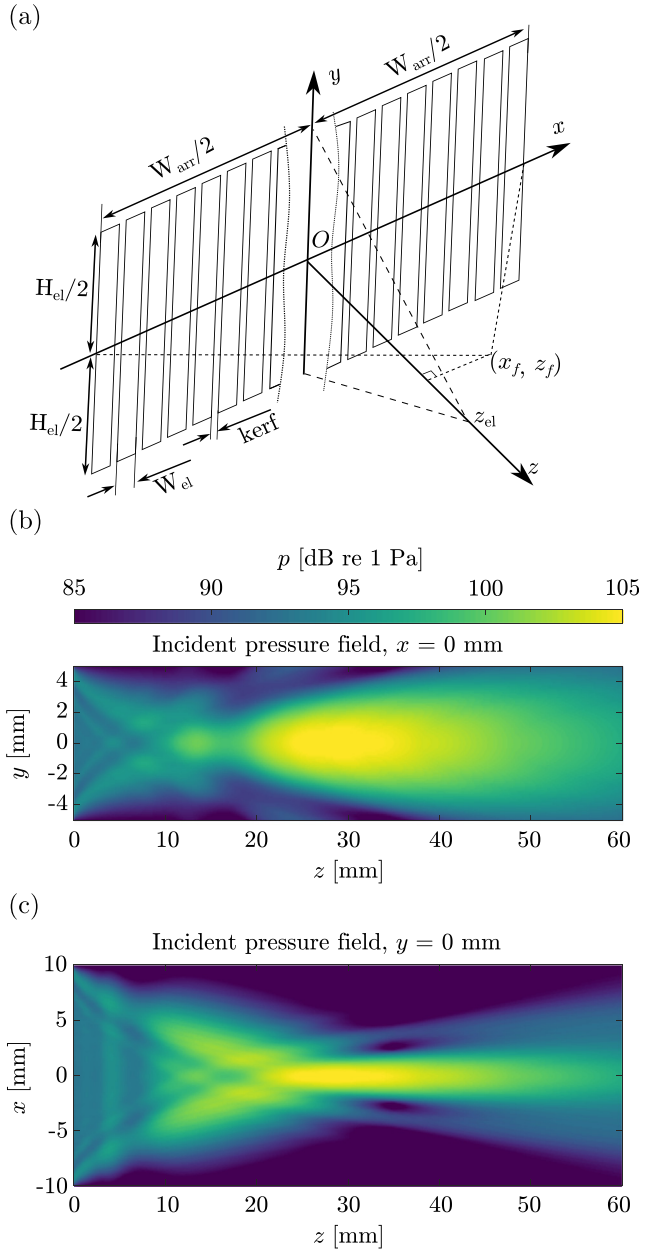

FIG. 6. (Color online) (a) Sketch of the geometry of the phased array used to generate the incident field. Maximum pressure of the incident beam generated by a phased array. (b) In the elevation plane $x = 0$ mm, and (c) in the azimuthal plane $y = 0$ mm.

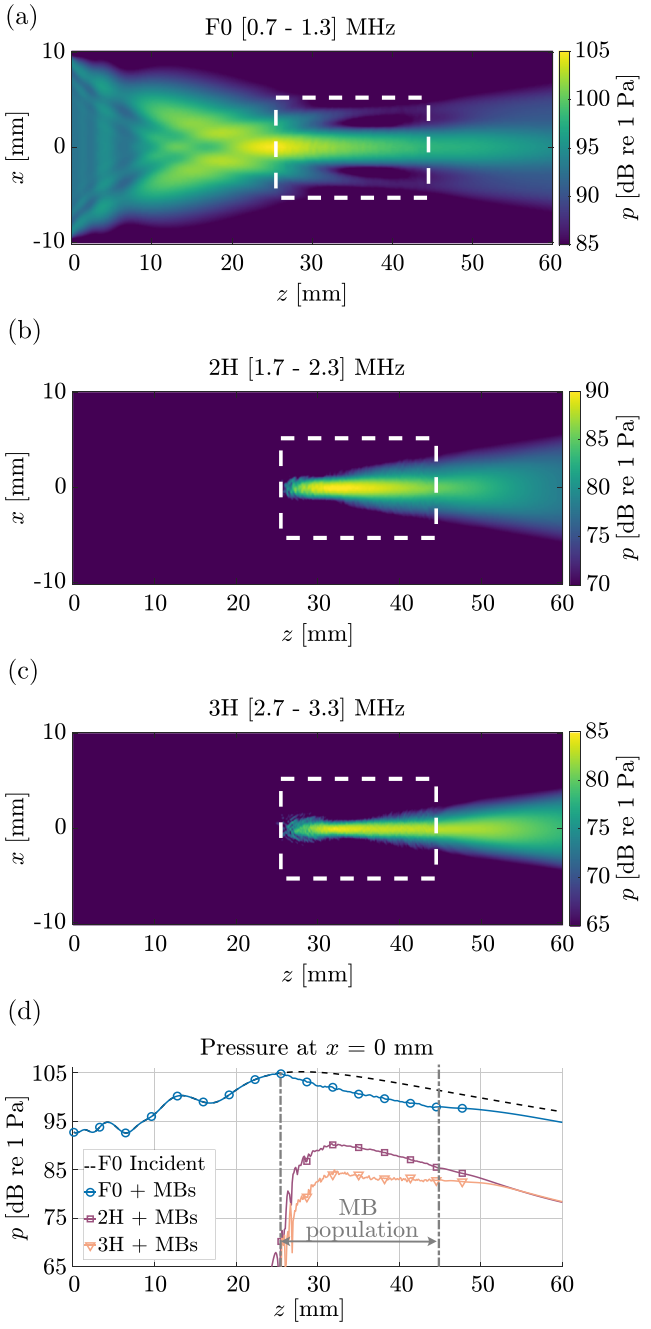

FIG. 7. (Color online) Spectral profiles at $y = 0$ mm for the beam generated by the phased array. (a) Fundamental), (b) second harmonic 2H, (c) third harmonic 3H for $j = 25$ iterations. The microbubble population is inside the dotted white rectangle. (d) Axial profiles of the harmonic beams. The dotted gray lines depict the location of the microbubble population.

The maximum of the emitted pressure is $P_0 = 50$ kPa at the surface, and the pressure is the highest and equal to 191 kPa at the focus. In Figs. 6(b) and 6(c), the incident beam is presented at the elevation plane $x = 0$ mm and the azimuthal plane $y = 0$ mm.

A population of 10^5 monodisperse microbubbles of 2 μm radius are randomly placed in a subdomain -5.30 mm $\leq x \leq 5.20$ mm, -2.55 mm $\leq y \leq 2.46$ mm, 25.5 mm $\leq z \leq 44.5$ mm, as indicated in Fig. 3. This means that the concentration of the microbubbles is about 10^5 ml^{-1}. The parameters for the Marmottant equation are the same as in Table I.

The results are depicted in Figs. 7(a)–7(c). The plots are made for $j = 25$ iterations, after which virtually no changes occur. The beam profiles of the harmonics are separated by using a 4th order Butterworth filter with cutoff frequencies indicated in the title of the plots. Because the embedding medium is linear, the higher harmonics are just caused by the microbubble population. In Figs. 7(a)–7(c), it is clearly visible that the 2H and 3H beams both come into existence at the point where the incident beam hits the bubble population. In the areas where the incident pressure is high, e.g., in the focal area of the incident beam, the microbubbles oscillate in a more nonlinear way, resulting in higher harmonic

Downloaded from http://pubs.aip.org/asa/jasa/article-pdf/153/4/2209/16822279/2209_1_10.0017770.pdf

https://doi.org/10.1121/10.0017770

pressures. There is 15 dB difference between the maximum pressure in the fundamental and 2H, whereas the difference between 2H and 3H is only about 5 dB. The latter can be explained by the fact that each microbubble simultaneously generates a number of higher harmonics. Since the microbubbles have a resonance frequency close to 3 MHz, both 2H and 3H will have about the same strength. These observations demonstrate that the mechanism of generating higher harmonics is quite different from the gradual growth of subsequent harmonics in case of medium nonlinearity. The difference between medium nonlinearity and nonlinearity caused by microbubbles also becomes manifest in the way the harmonics are generated by the iterative scheme. Loosely speaking, in case of medium nonlinearity, each iteration adds a new harmonic to the previous result,[24] and the full spectrum is only obtained after a number of iterations. In case of nonlinear microbubbles, even the first iteration yields the full scattering spectrum of the bubbles, and each iteration corrects the previous result by adding a new order of scattering. As shown in Fig. 5(d), the successive iterations do not cause large changes in the shape of the spectrum, but rather correct the overall amplitude.

Moreover, Fig. 7(d) depicts the axial profiles of the harmonic beams. Also, a comparison with the incident pressure field is presented. The pressure of the harmonics amplitude is lower than the pressure of the fundamental, as expected. In the area where the harmonic beams exist, the fundamental beam is lower than the incident beam, i.e., without microbubbles. This can be explained by the conversion of energy of the fundamental into energy of the higher harmonics.

In Figs. 8(a) and 8(b), a comparison between the fields of the first four orders of scattering are shown for two populations with concentrations of $10^5\,\mathrm{ml}^{-1}$ and $10^4\,\mathrm{ml}^{-1}$, respectively. For the higher concentration, the first three orders are of comparable amplitude. The peak amplitude of the fourth order is about 10 dB lower. On the other hand, for the lower concentration, the amplitude of the second scattering order is about 30 dB lower than the first. The third and

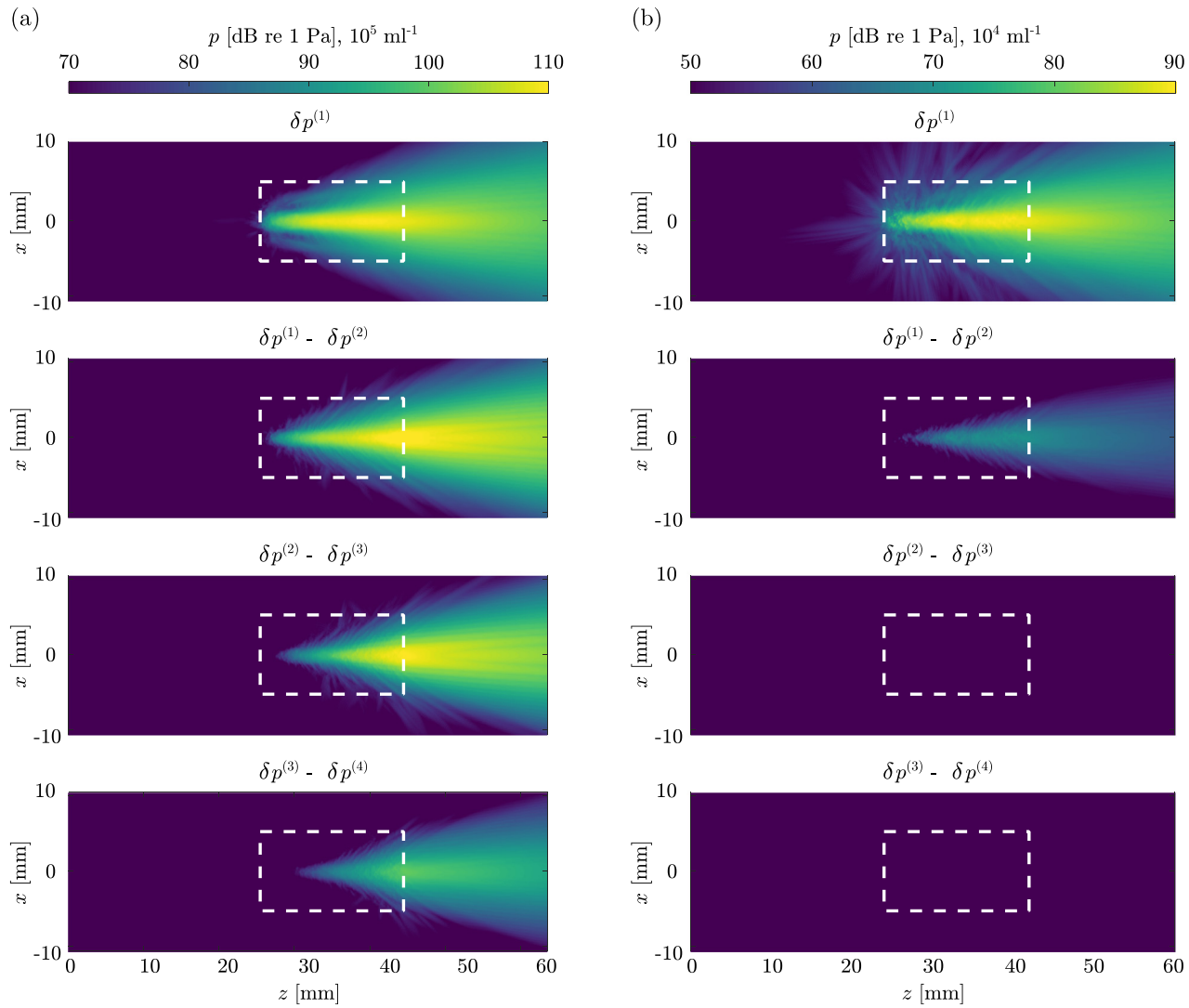

FIG. 8. (Color online) Beam profiles in the azimuthal plane $y = 0$ mm as generated by the phased array in a microbubble concentration of (a) $10^5\,\mathrm{ml}^{-1}$ and (b) $10^4\,\mathrm{ml}^{-1}$. The first, second, third, and fourth scattering orders are depicted from top to bottom, respectively. The microbubble population is inside the dotted white rectangle.

Downloaded from http://pubs.aip.org/asa/jasa/article-pdf/153/4/2209/16822279/2209_1_10.0017770.pdf

fourth scattering orders are at least 40 dB lower than the first order. Thus, these scattering orders do not significantly affect the final result. Finally, it is visible that the field of each scattering order is shifted to the left compared to the result of the previous order. This reinforces the fact that multiple scattering should be considered, especially for high concentrations.

D. Convergence

As illustrated in Fig. 2, each iteration adds an order of multiple scattering to the computed pressure field. This fact can be used to determine the dependence between the highest significant order of multiple scattering and the concentration of the microbubble population.

To determine the significance of an order of multiple scattering, we compare the results from the current iteration (j) and the previous iteration (j-1). The difference between these results over the spatial $\mathcal{X}_{\mathrm{cd}}$ and temporal $\mathcal{T}_{\mathrm{cd}}$ computational domain can be expressed by the RRMSE, which is defined as

$$\mathrm{RRMSE} = \sqrt{\frac{\int_{\mathcal{X}_{\mathrm{cd}}}\int_{\mathcal{T}_{\mathrm{cd}}}\left[p^{(j)}(\boldsymbol{x},t) - p^{(j-1)}(\boldsymbol{x},t)\right]^2 dt\, d\boldsymbol{x}}{\int_{\mathcal{X}_{\mathrm{cd}}}\int_{\mathcal{T}_{\mathrm{cd}}}\left[p^{(0)}(\boldsymbol{x},t)\right]^2 dt\, d\boldsymbol{x}}}. \tag{33}$$

After a number of iterations, the error will stabilize at a negligibly small level. In that case, we conclude that the addition of more scattering orders will not further improve the solution and we have reached the insignificant scattering orders. When this point has been reached, we say that the iterative process has converged.

In Fig. 9, the RRMSE as a function of the number of iterations j is depicted for several concentrations of the microbubble population. We observe that for higher concentrations, the initial iterations have a higher RRMSE. This indicates that the variations between the initial iterations increase with concentration. Moreover, we see that for higher concentrations, more iterations are needed to reach convergence. This can be explained by the fact that more close-range interactions occur in higher concentrations, making higher scattering orders more important.

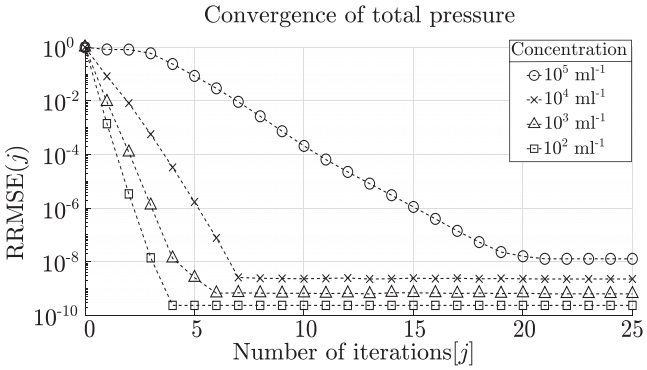

FIG. 9. RRMSE as a function of iterations for various populations of microbubbles concentrated in a volume of 1 ml.

VI. CONCLUSIONS

A novel method of simulating the multiple scattering of a pulsed ultrasound wave by a large 3D population of nonlinearly responding microbubbles was presented. The approach is based on the INCS method, which was extended to include a large number of nonlinear contrast point sources. Each of these act as a virtual volume injection source that generates the nonlinear scattering caused by an individual microbubble. The volume of each microbubble follows from its radius, which depends in a nonlinear way on the surrounding time dependent pressure, as described by the Marmottant model. Starting with the incident pressure from the primary transducer, the pressure in the four-dimensional (4D) spatiotemporal computational domain is successively updated by using a Neumann iterative scheme.

Physically, each iteration adds an extra order of multiple scattering between the microbubbles. Numerically, it takes several iterations before the difference between successive iterations stabilizes at a small number. From this, it was deduced that the inclusion of several orders of multiple scattering is necessary to accurately capture the behavior of a population of microbubbles. It was also observed that higher orders of multiple scattering become more important for increasing concentrations.

The developed method accounts for an accurate representation of the individual nonlinear behavior of each microbubble, as well as their higher order nonlinear interactions, and may therefore be used for detailed investigations into the behavior of realistic microbubble populations.

ACKNOWLEDGMENTS

This publication is part of the project "Optoacoustic sensor and ultrasonic microbubbles for dosimetry in proton therapy" of the Dutch National Research Agenda which is partly financed by the Dutch Research Council. The authors would like to thank Gonzalo Collado Lara, Nathan Blanken, Paul van Neer, and Nico de Jong for their fruitful discussions about this topic.

APPENDIX: SCATTERING BY A SMALL SPHERE

Here, we will show the steps that lead to Eqs. (15)–(17) in the main text. First, we shortly derive the exact scattering of a plane acoustical wave by a penetrable sphere of arbitrary size; extensive derivations may be found in the literature.[32] The plane wave has an angular frequency ω and is traveling in the z-direction through a medium with density of mass ρ_0 and speed of sound c_0. The sphere has a radius R, a mass density ρ_1, and a speed of sound c_1. For simplicity, the origin of the coordinate system is positioned at the center of the sphere. Using Cartesian coordinates with $\boldsymbol{x} = (x, y, z)$, the plane incident wave is

$$p_{\mathrm{inc}}(\boldsymbol{x},\omega) = p_0 \exp(-ik_0 z), \tag{A1}$$

where p_0 is the amplitude of the wave, and $k_0 = \omega/c_0$ is the wavenumber in the surrounding medium. To use the symmetry of the problem, we will turn to spherical coordinates

Downloaded from http://pubs.aip.org/asa/jasa/article-pdf/153/4/2209/16822279/2209_1_10.0017770.pdf

https://doi.org/10.1121/10.0017770

with $\boldsymbol{r} = (r, \theta, \phi)$, where r (radius) is the distance to the origin, θ (elevation) is the angle between the positive z-axis and the position vector, and ϕ (azimuth) is the angle between the positive x axis and the projection of the position vector on the xy-plane. In spherical coordinates, the incident wave becomes

$$p_{\text{inc}}(\boldsymbol{r}, \omega) = p_0 \sum_{n=0}^{\infty} a_n j_n(k_0 r), \tag{A2}$$

in which

$$a_n = (2n+1)(-i)^n P_n[\cos(\theta)]. \tag{A3}$$

In Eqs. (A2) and (A3), P_n is the n-th order Legendre polynomial and j_n is the spherical Bessel function of the first kind and order n. In analogy with Eq. (A2), the wave p_{sc} that is scattered by the sphere and the wave p_{tr} that is transmitted into the sphere can be written as

$$p_{\text{sc}}(\boldsymbol{r}, \omega) = p_0 \sum_{n=0}^{\infty} b_n h_n^{(2)}(k_0 r), \tag{A4}$$

$$p_{\text{tr}}(r, \omega) = p_0 \sum_{n=0}^{\infty} c_n j_n(k_1 r). \tag{A5}$$

Here, $h_n^{(2)}$ is the spherical Bessel function of the third kind and order n. The reflection coefficients b_n and the transmission coefficients c_n follow from the continuity of the pressure and the radial particle velocity at the boundary of the sphere, i.e., by requiring for each n that $p(\boldsymbol{r}, \omega)$ and $\rho^{-1}\partial p(\boldsymbol{r}, \omega)/\partial r$ are continuous at $r = R$. This yields

$$b_n = a_n \frac{\rho_0 c_0 j_n(k_0 R) j_n'(k_1 R) - \rho_1 c_1 j_n(k_1 R) j_n'(k_0 R)}{\rho_1 c_1 j_n(k_1 R) h_n^{(2)\prime}(k_0 R) - \rho_0 c_0 h_n^{(2)}(k_0 R) j_n'(k_1 R)}, \tag{A6}$$

$$c_n = a_n \frac{\rho_1 c_1 j_n(k_0 R) h_n^{(2)\prime}(k_0 R) - \rho_1 c_1 h_n^{(2)}(k_0 R) j_n'(k_0 R)}{\rho_1 c_1 j_n(k_1 R) h_n^{(2)\prime}(k_0 R) - \rho_0 c_0 h_n^{(2)}(k_0 R) j_n'(k_1 R)}, \tag{A7}$$

where the prime indicates the derivative of a function. Combination of Eqs. (A3), (A4), and (A6) yields the exact pressure that is scattered by the sphere.

Next, we consider the scattering by a sphere that is much smaller than the wavelength of the incident wave. In that case, it makes sense to represent the scattered pressure by its Taylor series around $R = 0$. If the frequency of the incident wave is much lower than the first resonance frequency of the sphere, it is sufficient to approximate the scattered pressure by the lowest order terms of the Taylor series. These are the terms of order R^3 that are given in Eqs. (15)–(17), where $p_0 = p(\boldsymbol{x}_{\text{sc}}, \omega)$ is the incident pressure at the location of the sphere. The term in Eq. (16) decays with r^{-2} and is negligible in the far field, which is dominated by the terms in Eqs. (15) and (17) with decay r^{-1}. The sum of these terms yields, after normalizing by $p_0 \exp(-ik_0 r)/4\pi r$, the well-known expression for the angle-distribution function of a nonrigid sphere in the long wavelength limit[32]

$$\Phi(\theta) = \frac{k^2 R^3}{3}\left[\frac{\kappa_1 - \kappa_0}{\kappa_0} + \frac{3(\rho_1 - \rho_0)}{2\rho_1 + \rho_0}\cos(\theta)\right]. \tag{A8}$$

[1]M. Versluis, E. Stride, G. Lajoinie, B. Dollet, and T. Segers, "Ultrasound contrast agent modeling: A review," Ultrasound Med. Biol. **46**, 2117–2144 (2020).
[2]N. de Jong, A. Bouakaz, and P. Frinking, "Basic acoustic properties of microbubbles," Echocardiography **19**, 229–240 (2002).
[3]J. W. S. Rayleigh, *The Theory of Sound* (Macmillan, London, UK, 1878).
[4]L. L. Foldy, "The multiple scattering of waves," Phys. Rev. **64**, 107–119 (1945).
[5]E. L. Carstensen and L. L. Foldy, "Propagation of sound through a liquid containing bubbles," J. Acoust. Soc. Am. **19**, 481–501 (1947).
[6]P. C. Waterman and R. Truell, "Multiple scattering of waves," J. Math. Phys. **2**, 512–537 (1961).
[7]A. L. Gower, M. J. A. Smith, W. J. Parnell, and I. D. Abrahams, "Reflection from a multi-species material and its transmitted effective wavenumber," Proc. R. Soc. A **474**, 20170864 (2018).
[8]L. van Wijngaarden, "On the equations of motion for mixtures of liquid and gas bubbles," J. Fluid Mech. **33**, 465–474 (1968).
[9]R. E. Calfish, M. J. Miksis, G. C. Papanicolaou, and L. Ting, "Effective equations for wave propagation in bubbly liquids," J. Fluid Mech. **153**, 259–273 (1985).
[10]C. Feuillade, "The attenuation and dispersion of sound in water containing multiply interacting air bubbles," J. Acoust. Soc. Am. **99**, 3412–3430 (1996).
[11]F. S. Henyey, "Corrections to Foldy's effective medium theory for propagation in bubble clouds and other collections of very small scatterers," J. Acoust. Soc. Am. **105**, 2149–2154 (1999).
[12]C. Feuillade, "Acoustically coupled gas bubbles in fluids: Time-domain phenomena," J. Acoust. Soc. Am. **109**, 2606–2615 (2001).
[13]K. W. Commander and A. Prosperetti, "Linear pressure waves in bubbly liquids: Comparison between theory and experiments," J. Acoust. Soc. Am. **85**, 732–746 (1989).
[14]L. D'Agostino and C. Brennen, "Linearized dynamics of spherical bubble clouds," J. Fluid Mech. **199**, 155–176 (1989).
[15]S. Kumar and C. Brennen, "Nonlinear effects in the dynamics of clouds of bubbles," J. Acoust. Soc. Am. **89**, 707–714 (1991).
[16]Z. Ye and L. Ding, "Acoustic dispersion and attenuation relations in bubbly mixture," J. Acoust. Soc. Am. **98**, 1629–1636 (1995).
[17]E. Stride and N. Saffari, "Investigating the significance of multiple scattering in ultrasound contrast agent particle populations," IEEE Trans. Ultrason., Ferroelectr. Freq. Control **52**, 2332–2345 (2005).
[18]K. Hibbs, J.-M. Mar, E. Stride, R. Eckersley, A. Noble, and M.-X. Tang, "Nonlinear propagation of ultrasound through microbubble clouds: A novel numerical implementation," in *Proceedings of the 2007 IEEE Ultrasonics Symposium* (2007), pp. 1997–2000.
[19]N. C. Ovenden, J. O'Brienn, and E. Stride, "Ultrasound propagation through dilute polydisperse microbubble suspensions," J. Acoust. Soc. Am. **142**, 1236–1248 (2017).
[20]V. Leroy, A. Strybulevych, M. G. Scanlon, and J. H. Page, "Transmission of ultrasound through a single layer of bubbles," Eur. Phys. J. **29**, 123–130 (2009).
[21]O. Lombard, C. Barrière, and V. Leroy, "Nonlinear multiple scattering of acoustic waves by a layer of bubbles," EPL **112**, 24002 (2015).
[22]A. Joshi, B. D. Lindsey, P. A. Dayton, G. Pinton, and M. Muller, "An iterative fullwave simulation approach to multiple scattering in media with randomly distributed microbubbles," Phys. Med. Biol. **62**, 4202–4217 (2017).
[23]J. Huijssen, "Modeling of nonlinear medical diagnostic ultrasound," Ph.D. thesis, Delft University of Technology, Netherlands, 2008.
[24]J. Huijssen and M. D. Verweij, "An iterative method for the computation of nonlinear, wide-angle, pulsed acoustic fields of medical diagnostic transducers," J. Acoust. Soc. Am. **127**, 33–44 (2010).
[25]M. D. Verweij and J. Huijssen, "A filtered convolution method for the computation of acoustic wave fields in very large spatio-temporal domains," J. Acoust. Soc. Am. **125**, 1868–1878 (2009).
[26]M. D. Verweij, "Modeling space-time domain acoustic wave fields in media with attenuation: The symbolic manipulation approach," J. Acoust. Soc. Am. **97**, 831–843 (1995).

Downloaded from http://pubs.aip.org/asa/jasa/article-pdf/153/4/2209/16822279/2209_1_10.0017770.pdf

[27]M. D. Verweij, "Transient acoustic wave fields in continuously layered media with depth-dependent attenuation: An analysis based on higher-order asymptotics," J. Acoust. Soc. Am. **101**, 1808–1820 (1997).
[28]L. Demi, M. D. Verweij, J. Huijssen, N. de Jong, and K. W. A. van Dongen, "Attenuation of ultrasound pressure fields described via a contrast source formulation," in *Proceedings of 2009 IEEE Ultrasonics* (2009), pp. 1590–1593.
[29]L. Demi, K. W. A. van Dongen, and M. D. Verweij, "A contrast source method for nonlinear acoustic wave fields in media with spatially inhomogeneous attenuation," J. Acoust. Soc. Am. **129**, 1221–1230 (2011).
[30]J. Huijssen, M. D. Verweij, and N. de Jong, "Modeling nonlinear three-dimensional pulsed acoustic fields in diagnostic ultrasound including tissue-like attenuation," in *Proceedings of 2008 IEEE Ultrasonics* (2008), pp. 375–378.
[31]P. Marmottant, S. van der Meer, M. Emmer, M. Versluis, N. de Jong, S. Hilgenfeldt, and D. Lohse, "A model for large amplitude oscillations of coated bubbles accounting for buckling and rupture," J. Acoust. Soc. Am. **118**, 3499–3506 (2005).
[32]P. F. Morse and K. U. Ingard, *Theoretical Acoustics* (McGraw-Hill, New York, 1968).
[33]M. F. Hamilton and D. T. Blackstock, *Nonlinear Acoustics* (Academic Press, San Diego, 1998).
[34]A. T. de Hoop, *Handbook of Radiation and Scattering of Waves* (Academic Press, San Diego, 1995).
[35]A. C. Hindmarsh, "ODEPACK, A Systematized Collection of ODE Solvers," IMACS Trans. Sc. Comp. **1**, 55–64 (1983).
[36]E. S. Wise, B. T. Cox, J. Jaros, and B. E. Treeby, "Representing arbitrary acoustic source and sensor distributions in Fourier collocation methods," J. Acoust. Soc. Am. **146**, 278–288 (2019).

Downloaded from http://pubs.aip.org/asa/jasa/article-pdf/153/4/2209/16822279/2209_1_10.0017770.pdf